frontiers | Frontiers in Physics

TYPE Original Research
PUBLISHED 05 February 2024
DOI 10.3389/fphy.2023.1302254

OPEN ACCESS

EDITED BY
Wei Zhao,
Northwest University, China

REVIEWED BY
V. N. Du Le,
The University of Alabama in Huntsville, United States
Radu Hristu,
Polytechnic University of Bucharest, Romania

*CORRESPONDENCE
Alexander Ushenko,
o.ushenko@chnu.edu.ua
Jun Zheng,
dbzj@netease.com

RECEIVED 26 September 2023
ACCEPTED 29 December 2023
PUBLISHED 05 February 2024

CITATION
Ushenko A, Dubolazov A, Zheng J, Bakun O, Gorsky M, Ushenko Y, Litvinenko O, Gordey I, Zhebo C and Sklyarchuk V (2024), Mueller matrix polarization interferometry of optically anisotropic architectonics of biological tissue object fields: the fundamental and applied aspects.
Front. Phys. 11:1302254.
doi: 10.3389/fphy.2023.1302254

Mueller matrix polarization interferometry of optically anisotropic architectonics of biological tissue object fields: the fundamental and applied aspects

Alexander Ushenko[1,2]*, Alexander Dubolazov[2], Jun Zheng[1]*, Oxana Bakun[3], Mykhaylo Gorsky[2], Yuriy Ushenko[4], Olexandra Litvinenko[3], Ivan Gordey[4], Chen Zhebo[1] and Valeriy Sklyarchuk[2]

[1]Photoelectric Information Center, Taizhou Institute of Zhejiang University, Taizhou, China, [2]Optics and Publishing Department, Chernivtsi National University, Chernivtsi, Ukraine, [3]Department of Forensic Medicine and Medical Jurisprudence, Bucovinian State Medical University, Chernivtsi, Ukraine, [4]Computer Science Department, Chernivtsi National University, Chernivtsi, Ukraine

The presented results concern the diagnostic application of vector-parameter polarization mapping and polarization-interference phase scanning applied to layered azimuths and ellipticity polarization maps obtained with the help of digital holographic reproduction for phase-inhomogeneous tissue layers in the female reproductive system. The differential diagnosis of the pathological changes in optically anisotropic polycrystalline tissue components, specifically "benign (fibroids) and precancerous (endometriosis)," was investigated. All studies within the representative groups of the histological samples were conducted using circularly polarized laser radiation, ensuring azimuthal invariance and polarization measurement reliability. Integral and layered maps and polarization azimuths and ellipticity random variable distribution histograms were obtained from the microscopic images of histological sections from the female reproductive system tumors. Systematized tables present statistical moments which characterize azimuths and ellipticity polarization maps for fibroids and endometriosis tissues. It is shown that the statistical parameters (diagnostic markers) are the most sensitive to benign and precancerous changes in the female reproductive system tissues. The results of information analysis, including the accuracy determination of the diagnostic vector-parameter polarization and polarization-interference methods for detecting and differentiating the samples of fibroids and precancerous endometriosis tissues in the female reproductive system, are presented.

KEYWORDS

polarization, interference, holography, microscopic image, optical anisotropy, statistical moments, balanced accuracy, female reproductive system

1 Introduction

Enhancing the capacity to detect cancer in the female reproductive system, particularly in the early preclinical stages such as endometriosis, is a crucial aspect of addressing the global challenge of "sustainable development." Endometriosis involves the growth of tissues resembling the uterine inner layer outside the uterus, leading to pain and potential infertility [1]. Worldwide, endometriosis affects approximately 10% (190 million) of women and girls of reproductive age [2]. It is a chronic disease, with symptoms such as severe, interfering pain during menstruation, intercourse, defecation, and/or urination; chronic pelvic pain; abdominal bloating; nausea; increased fatigue; and sometimes, also depression, anxiety disorder, and infertility. Because of the variety of symptoms of endometriosis, it is not easy for health professionals to diagnose the disease, and many people who suffer from it know little about it. Therefore, it sometimes takes quite a long time from the onset of symptoms to diagnosis [3]. Currently, there is no universally recognized treatment for endometriosis, and in most cases, treatment is limited to the elimination of symptoms [4].

In recent years, modern optical–physical methods of oncological diagnostics have progressed. A significant achievement in this field was the development of polarization-sensitive optical coherence tomography (PSOCT) techniques which have become promising in this direction. The basic principles and achievements of the PSOCT of biological objects over the past 25 years have been consistently set out in a series of review articles [5–7]. This laser polarization-interference technique not only makes it possible to obtain layered images from small depths (up to 2 mm) of biological tissues [8, 9] but also provides the possibility of obtaining coordinate distributions of the Jones and Mueller matrix elements and anisotropy maps. This was most effectively demonstrated in studies of transparent eye tissues [10–12].

PSOCT functionality has been extended with the studies of layered polarization and matrix images of radiation which was scattered (depolarized) on the biological tissues of various morphological structures and physiological states [8]. In particular, it was possible to accurately diagnose fibrosis and differentiate tumor sites with low fibrosis [13], along with benign and malignant tumors of the larynx [14]. However, the sensitivity and resolution of such systems was limited due to the distortion effect produced by the high level of depolarized laser speckle background. This leads to low contrast for polarizing images which are obtained by such tissue-layer illumination.

Based on this, the creation and development of high-resolution (0.5 μm–1 μm) polarization-interference microscopy systems, which functionally complement PSOCT techniques, is relevant. This technique, combined with digital holographic phase scanning of a multiple-scattered object field, can not only significantly increase the contrast of polarization images but also provide a Mueller matrix reconstruction of the optical anisotropy parameters for the samples, such as histological biological tissue sections.

To address the aforementioned challenges, further fundamental and applied development of optical diagnostic methods is needed. The desired results can be achieved by integrating modern laser polarimetry techniques [15–21] based on Mueller matrix formalism [22–29] and digital holography [30–33], which provide exhaustive information about the layered optical anisotropic hierarchical structure of biological tissues. The promising initial results have been demonstrated in the high-precision (~95%) comprehensive early detection of prostate cancer using layered Mueller matrix mapping [32].

However, the obtained results remain somewhat empirical. Currently, there is no information about the possibilities with this method for the samples with different optical thicknesses, morphological structures, and various pathologies. From a physical point of view, the task is to form relationships between the structure of polycrystalline networks of biological tissues and the layered distribution of polarization parameters (azimuth and ellipticity).

Our research will concentrate on advancing a novel and logically complementary PSOCT method that combines Mueller matrix interferometry with the microscopic imaging of the histological sections which are made from diverse biological tissues. These sections exhibit various morphological structures and physiological states. Methodologically, this approach relies on a comprehensive Mueller matrix model to characterize the morphological structure of biological tissues. In this model, the biological tissues are conceptualized as amorphous and polycrystalline structures [20, 21]. The polarization distributions of azimuths and ellipticity in the microscopic image of biological tissues are shaped by the polycrystalline component. From a crystal-optical perspective, this component is regarded as a combination of the structural mechanisms (such as linear birefringence and dichroism in fibrillar networks composed of diverse protein molecules, such as collagen, myosin, and elastin) and chiral mechanisms (involving circular birefringence and dichroism in optically active protein complexes with molecular chiral rings) [34–36].

The amorphous component of biological tissue consists of fats, lipids, biochemical acids, and other optically inactive molecules. Its impact on the object field parameters is characterized by the absorption and attenuation of optical radiation. The proposed Mueller matrix interferometry technique is a technological synthesis which incorporates the Mach–Zehnder polarization-interference platform, digital holographic reconstruction, and step-by-step phase scanning to analyze complex amplitude distributions in the microscopic images of biological tissue histological sections.

Consequently, our approach introduces a novel capability for experimentally implementing the phase selection of laser radiation components with varying scattering multiplicities. This allows for the isolation of an informatively relevant "low-fold" or single-scattered polarization component in microscopic images. The distributions of polarization parameters (azimuths and ellipticity) in this component are maximally and unambiguously correlated with the structural parameters of the polycrystalline component in the native biological tissue section. The anticipated outcomes include a substantial enhancement in method sensitivity and the provision of contemporary diagnostic insights in the pathological changes within depolarizing biological layers' polycrystalline components.

Our research is concentrated on advancing and experimentally validating Mueller matrix polarization-interferometry methods for characterizing multiple scattered fields in diffusive biological tissue layers within the female reproductive system. The objective is to investigate the potential of the layered digital holographic selection of components with varying scattering multiplicities in the polarization-inhomogeneous field. This leads to the enhanced accuracy of the differential diagnosis between benign conditions, such as fibroids and precancerous tissues, specifically endometriosis, within the female reproductive system.

2 Materials and methods

In this section, we will briefly review (without reducing the completeness of the analysis) the main theoretical relationships within the framework of the linear birefringence (*LB*) approximation. It describes the processes of polarization structure formation in the cases of single- and multiple-radiation scattering on diffusive tissue layers. This allows us to calculate the amount of object laser field components formed by the histological sections of the female reproductive system with benign and precancerous changes.

2.1 Object field Stokes polarimetry

To obtain reliable (azimuthally invariant) information within the representative histological sections of the tissue biopsy samples from the female reproductive system, illumination is performed using right-circularly (⊗) polarized beams with an azimuth angle α_0. The Stokes vector of this polarized beam is given by the following expression [15–19] (Eq. 1):

$$VS^0(\otimes) = \begin{pmatrix} 1 \\ 0 \\ 0 \\ 1 \end{pmatrix}. \tag{1}$$

2.1.1 "Single-scattering" interaction

The polarization properties of an optically anisotropic (Δn, the index of linear birefringence, *LB*) protein fibril (with a geometric size d and spatial orientation of the optical axis ρ) in the volume of the tissue sample from the female reproductive system are represented by a Mueller matrix birefringence operator [16, 19] (Eq. 2):

$$\{W\}_j = \begin{pmatrix} 1 & 0 & 0 & 0 \\ 0 & \omega_{22} & \omega_{23} & \omega_{24} \\ 0 & \omega_{32} & \omega_{33} & \omega_{34} \\ 0 & \omega_{42} & \omega_{43} & \omega_{44} \end{pmatrix}_j =$$

$$= \begin{pmatrix} 1 & 0 & 0 & 0 \\ 0 & (\cos^2 2\rho + \sin^2 2\rho \cos\delta) & (\cos 2\rho \sin 2\rho(1-\cos\delta)) & (\sin 2\rho \sin\delta) \\ 0 & (\cos 2\rho \sin 2\rho(1-\cos\delta)) & (\sin^2 2\rho + \cos^2 2\rho \cos\delta) & (\cos 2\rho \sin\delta) \\ 0 & (\sin 2\rho \sin\delta) & (\cos 2\rho \sin\delta) & (\cos\delta) \end{pmatrix}_j. \tag{2}$$

Here, $\delta = \frac{2\pi}{\lambda}\Delta n d$ is the phase shift between the linearly orthogonally polarized components of the laser beam amplitude, where λ is the wavelength.

The process of single-scattering transformation through the polarization structure of the probing beam $S^0(\otimes)$ by a local (ith) fibril $(\rho_j; \delta_j)$ is described by the following matrix equation:

$$VS_i^*(\alpha_i, \beta_i) = \{W\}_i VS^0(\otimes). \tag{3}$$

As a result, a wave, which is formed as a result of a local act of scattering, can be described with the following azimuth α_i and ellipticity β_i of polarization (Eqs 4, 5):

$$\alpha_j = 0.5\, arctan\left(VS_3^*/VS_2^*\right) = 0.5\, arctan\left(cotan 2\rho_j\right) \equiv q\left(\rho_j\right), \tag{4}$$

$$\beta_j = 0.5 arcsin\left(VS_4^*/VS_1^*\right) = 0.5 arcsin\left(\cos\delta_j\right) \equiv g\left(\delta_j\right). \tag{5}$$

Here, $VS^*_{i=1;2;3;4}$ represents the parameters of the Stokes vector of the singly scattered laser beam $VS_i^*(\alpha_j, \beta_j)$. Thus, the singly scattered component in the object field of the protein fibrillar network in the tissue of the female reproductive system constitutes two polarization distributions:

- "Azimuthal-orientational" distribution denoted by $\Lambda(\alpha_j; \rho_j)$
- "Phase" distribution denoted by $\Psi(\beta_j; \delta_j)$

2.1.2 "n-fold" interaction

For multiple interactions with the protein fibrillar network in the female reproductive system, matrix Eq. 3 for a circularly polarized laser probe $VS^0(\otimes)$ takes the following form [20, 21] (Eqs 6–8):

$$VS_j^n\left(\alpha_j^n; \beta_j^n\right) = \{W\}_n \{W\}_{n-1} \ldots \{W\}_2 \{W\}_1 VS^0(\otimes). \tag{6}$$

This optical scenario generates an ensemble of the following random values of azimuth α_j^n and ellipticity β_j^n:

$$\alpha_j^n = 0.5\, arctan\left(\sum_{j=1}^n VS_{3j}^* \Big/ \sum_{j=1}^n VS_{2j}^*\right) \equiv \sum_{j=1}^n q\left(\rho_j\right), \tag{7}$$

$$\beta_j^n = 0.5\, arcsin\left(\sum_{j=1}^n VS_{4j}^* \Big/ \sum_{j=1}^n VS_{1j}^*\right) \equiv \sum_{j=1}^n g\left(\delta_j\right). \tag{8}$$

As a result, a polarization-variant component of the diffuse field will be formed with a different distribution of the azimuthal $\Lambda^n(\sum_{j=1}^n q(\rho_j))$ and ellipticity values $\Psi^n(\sum_{j=1}^n g(\delta_j))$ of polarization.

Thus, the polarization structure $\mathrm{P}^n(\alpha^n; \beta^n)$ for the laser field, which was multiply scattered in the tissue of the female reproductive system, can be represented as the superposition of "orientational" and "phase" components (Eq. 9).

$$\mathrm{P}^n(\alpha^n; \beta^n) = \Lambda^n\left(\sum_{j=1}^n q\left(\rho_j\right)\right) + \Psi^n\left(\sum_{j=1}^n g\left(\delta_j\right)\right). \tag{9}$$

The coherence of laser radiation facilitates an alternative analytical description. It is focused on the amplitude aspects of the processes shaping the probing field within the polarization structure of the diffuse layers in female reproductive tissue.

2.1.3 Amplitude analysis

For coherent laser fields, there exists a direct relationship between the parameters of the Stokes vector and the orthogonal components (U_{xj} and U_{yj}) of complex amplitudes [33]. Based on this, the previously obtained expressions (4 and 5) for the polarization parameters can be rewritten as follows (Eqs 10, 11):

$$\alpha_j\left(\rho_j\right) = 0.5\, arctan\left(\left(U_{xj}U_{yj}^* + U_{xj}^* U_{yj}\right) \Big/ \left(U_{xj}U_{xj}^* - U_{yj}U_{yj}^*\right)\right), \tag{10}$$

$$\beta_j\left(\delta_j\right) = 0.5 arcin\left(i\left(U_{xj}U_{yj}^* - U_{xj}^* U_{yj}\right) \Big/ \left(U_{xj}U_{xj}^* + U_{yj}U_{yj}^*\right)\right). \tag{11}$$

Indeed, in parallel with this scenario, another process takes place: the interference summation of differently polarized partial coherent waves, leading to the formation of another polarization-

variant component in the object field which is scattered by the female reproductive diffuse tissue section.

2.1.4 Interference interaction

For the orthogonal components U_{xj} and U_{yj} of the complex amplitudes U_1 and U_2, respectively, of two partially singly scattered coherent waves at a local point in the object field, the following interference equations can be written (Eqs 12, 13):

$$U_{xj} = (U_{x1} + U_{x2})_j = \left(|U_{x1}| + |U_{x2}| + 2\sqrt{|U_{x1}||U_{x2}|}\cos\varphi_{x12}\right)_j, \quad (12)$$

$$U_{yj} = \left(U_{y1} + U_{y2}\right)_j = \left(\left|U_{y1}\right| + \left|U_{y2}\right| + 2\sqrt{\left|U_{y1}\right|\left|U_{y2}\right|}\cos\varphi_{y12}\right)_j, \quad (13)$$

where $|U_{xj}|; |U_{yj}|$ are the modules of complex amplitudes and φ_{x12} and φ_{y12} are the phase shifts between $(U_{x1}; U_{x2})$ and $(U_{y1}; U_{y2})$, respectively.

The following equations can be written for the resulting orthogonal components of amplitudes U_x and U_y due to the "n-fold" interaction in the scattering process of the laser probe with optical heterogeneities (Eq. 14):

$$U_x = \sum_{j=1}^{n} U_{xj}; U_y = \sum_{j=1}^{n} U_{yj}; \varphi_{xy} = \sum_{i=1}^{n} \varphi_{xj} - \sum_{i=1}^{n} \varphi_{yj}. \quad (14)$$

The interference addition of two phase-shifted orthogonal components U_x and U_y by a phase difference φ_{xy} results in an elliptically polarized wave [24] (Eq. 15):

$$\frac{X^2}{U_x^2} + \frac{Y^2}{U_y^2} - \frac{2XY}{U_x U_y}\cos\varphi_{xy} = \sin^2\varphi_{xy}, \quad (15)$$

with the following "interference" values (I) of azimuth $\alpha(I)$ and ellipticity $\beta(I)$:

$$\alpha(I) = 0.5\arcsin\left(\sin 2\left(\frac{U_y}{U_x}\right) \Big/ \sqrt{1 + \tan^2\delta_{xy}\cos^2 2\left(\frac{U_y}{U_x}\right)}\right), \quad (16)$$

$$\beta(I) = 0.5\arctan\left(\tan\delta_{xy}\sin 2\left(\frac{U_y}{U_x}\right) \Big/ \sqrt{1 + \tan^2\delta_{xy}\cos^2 2\left(\frac{U_y}{U_x}\right)}\right). \quad (17)$$

As we can see, because of the secondary interference of differently polarized coherent partial waves, a polarization-inhomogeneous component (denoted as $\Lambda I(\alpha_j^n)$ and $\Psi I(\beta_j^n)$) is also formed (according to Eqs. 16, 17). An object field is produced by the scattering on biological tissues from the female reproductive sphere.

2.1.5 Resulting field

Thus, the polarization structure of the laser field, scattered by the female reproductive sphere tissues, can be represented as the superposition of the following components:

$$\Phi(\alpha;\beta) = \left\{\Lambda\left(\alpha_j;\rho_j\right) + \Psi\left(\beta_j;\delta_j\right)\right\} + \Lambda^n\left(\sum_{j=1}^{n} q\left(\rho_j\right)\right) + \Psi^n\left(\sum_{j=1}^{n} g\left(\delta_j\right)\right) + \left\{\Lambda I\left(\alpha_j^n;\varphi_j\right) + +\Psi I\left(\beta_j^n;\varphi_j\right)\right\}. \quad (18)$$

3 Experimental setup and measurement methodology

The Stokes-polarimetric mapping scheme based on the Mach–Zehnder interferometer is a generalization of the polarization-interferometry scheme [30–33], which is shown in Figure 1.

The parallel ($\boldsymbol{Ø = 2000\,\mu m}$) illuminating ("probing") beam of He–Ne ($\boldsymbol{\lambda = 0.6328\mu m}$) laser (1), formed by the spatial-frequency filter (2), with a 50% beam splitter (3) is divided into "object" and "reference" ones. The "object" beam with the help of a rotating mirror (5) is directed through the polarizing filter (6–7), which forms a right-circularly polarized beam [relation (1)]. Next, such an "object" beam is sent in the direction of the female biological tissue histological section layer (8). The polarization-inhomogeneous image of the biological tissue histological sections (8) is projected by the strain-free objective (12) into the digital camera (14) plane.

The "reference" beam is directed by the mirror (4) through the polarization filter (9–10), which forms its right-circular state

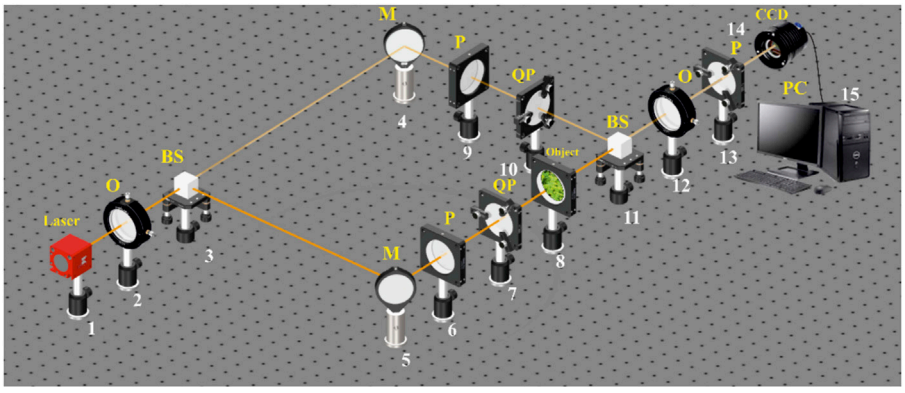

FIGURE 1
Optical scheme for polarization-interference mapping of the Stokes vector parameters.1: He–Ne laser; 2: collimator—"O"; 3 and 11: beam splitters—"BS"; 4 and 5: mirrors—"M"; 6, 9, and 13: polarizers—"P"; 7 and 10: quarter wave plates—"QP"; 8: object; 12: polarization objective—"O"; 14: digital camera—"CCD"; and 15: personal computer—"PC."

of polarization. The resulting beam is sent into the polarization-inhomogeneous image plane histological sections (8), which forms the microscopic image. Next, a circularly polarized "reference" wave using a beam splitter (11) and a polarizing lens (12) is superimposed on a microscopic image of a native histological section of female biological tissue. As a result, an interference pattern is formed, the coordinate intensity distribution of which is recorded using a digital camera (14) through a polarizer (13).

Before carrying out the measurements of biological tissues, the experimental device passed the metrological certification with the introduction of model objects ("clean air," "linear polarizer," and "phase plates $\mathbf{0.25\lambda}$" and "$\mathbf{0.5\lambda}$"). For each type of model object, 50 measurements of ellipticity were carried out. Within each series of measurements, the average (mathematical expectation) and the standard deviation of the measured values were determined according to the standard methodology of probability theory. As a result, the final value of the standard deviation was $\boldsymbol{\beta = 0.0003\ rad}$.

The methodology, for a layer-by-layer measurement of the object field Stokes vector-parameter (polarization maps $\boldsymbol{\alpha(m,n)}$ and $\boldsymbol{\beta(m,n)}$) distributions, is using complex amplitudes $\boldsymbol{E_x}$ and $\boldsymbol{E_y}$ from a digital holographic reconstruction, followed by the phase scanning $\boldsymbol{\theta_k}$ of an object field. It is presented in [30–33]. However, detailed information is not provided in this work. For a better understanding of the further discussion, we provide a brief overview of the 3D digital holographic scanning method.

4 The method of 3D polarimetry phase scanning of the object field

1. Using polarizing filters (6–7) and (9–10), circular polarization (⊗) is sequentially formed in the "irradiating" (Ir) and "reference" (Re) parallel laser beams, $Ir(\otimes) - Re(\otimes)$.
2. For the circular polarization (⊗) state, two partial interference patterns are recorded through the polarizer–analyzer (14) with the orientation of the transmission plane at angles $\Omega = 0^0;\ \Omega = 90^0$.
3. The analytical processing of female biological tissue histological section microscopic interference images was carried out using the digital Fourier transform $FT(\upsilon,\nu)$ [30–33] (Eq. 19):

$$FT_{x;y}(\upsilon,\nu) = \frac{1}{M\times N}\sum_{m=0}^{M-1} \times\sum_{n=0}^{N-1} I_{x,y}(\Omega = 0^0;90^0)(m,n)exp\left[-i2\pi\left(\frac{m\times\upsilon}{M}+\frac{n\times\nu}{N}\right)\right], \tag{19}$$

where $\{I_x^{\otimes}(\Omega = 0^0)(m,n) = U_x^{\otimes}(\Omega = 0^0)(U_x^{\otimes})^*(\Omega = 0^0)(m,n);$ $I_y^{\otimes}(\Omega = 90^0)(m,n) = U_y^{\otimes}(\Omega = 90^0)(U_y^{\otimes})^*(\Omega = 90^0)(m,n); U_{x,y}^{\otimes}$ are the orthogonal components of complex amplitude for different orientations $\Omega = 0^0;\ \Omega = 90^0$; * denotes the complex conjugation operation; (υ,ν) are the spatial frequencies; and $(m = 1120;\ n = 960)$ are the quantity of pixels of the CCD camera.

4. The results of the digital Fourier transform (relation (18)) are used to obtain complex amplitude distributions according to the following algorithms (Eq. 20, 21):

$$U_{0^0} \rightarrow \left|U_x^{\otimes}(\Omega = 0^0)\right|, \tag{20}$$

$$U_{90^0} \rightarrow \left|U_y^{\otimes}(\Omega = 90^0)\right| exp\left(i\left(\varphi_x^{\otimes} - \varphi_y^{\otimes}\right)\right). \tag{21}$$

5. By the means of the stepwise $(\Delta\theta)$-phase (θ_k) scanning of the reconstructed complex amplitude (relations (20) and (21)) field using algorithms (10)–(11), we obtain polarization parameters $\alpha(\theta_k,m,n)$ and $\beta(\theta_k,m,n)$ coordinate distributions.
6. The resulting set of polarization maps $p \equiv \begin{cases}\alpha(\theta_k,m,n);\\ \beta(\theta,m,n)\end{cases}$ was analyzed in a statistical approach using the following algorithms to calculate the mean (Z_1), variance (Z_2), skewness (Z_3), and kurtosis (Z_4) [20, 21] (Eq. 22):

$$\begin{aligned} Z_1 &= \frac{1}{K}\sum_{j=1}^{K} p_j;\\ Z_2 &= \sqrt{\frac{1}{K}\sum_{j=1}^{K}(p^2)_j};\\ Z_3 &= \frac{1}{Z_2^3}\frac{1}{K}\sum_{j=1}^{K}(p^3)_j;\\ Z_4 &= \frac{1}{Z_2^4}\frac{1}{K}\sum_{j=1}^{K}(p^4)_j, \end{aligned} \tag{22}$$

where K is the CCD pixel quantity.

7. By reducing the magnitude of the phase parameter θ_k, the "boundary" value θ_k^* is determined to isolate the biological object field single-scattered component, starting from which the aggregate $Z_{i=1;2;3;4}(\alpha(\theta_k^*,m,n)) \approx const$ and $Z_{i=1;2;3;4}(\beta(\theta_k^*,m,n)) \approx const$.

5 Object of investigations

The objects of the study were native histological sections of the endometrium, which were prepared according to the standard procedure using a microtome with rapid freezing.

Optically thin (group 1) and optically thick (group 2) samples of histological sections were created, including specimens with benign and precancerous changes in the female reproductive tissue. These samples were used to conduct a comparative analysis of the diagnostic efficiency of the Mueller matrix method under the conditions of scattering with varying multiplicities.

The optical-geometric parameters of the samples are presented in Table 1.

The measurement of the uterine tissue sample extinction coefficient was carried out according to the standard procedure of light attenuation

TABLE 1 Female reproductive system histological section optical and geometric parameters.

Parameter	Optically thin	Optically thick
Geometric thickness $h, \mu m$	20–25	40–45
Optical thickness $\tau, \mu m$	0.093–0.012	0.14–0.18
Degree of depolarization $\Delta, \%$	6–9	27–32

measurement [37] using an integral light-scattering sphere [38, 39]. The sample preparation procedure was conducted in accordance with the principles of the Declaration of Helsinki and in compliance with the International Conference on Harmonization, Good Clinical Practice and local regulatory requirements. The study was reviewed and approved by the appropriate independent ethics committees.

Within groups 1 and 2, two representative subgroups of the histological section samples were formed:

1. Benign samples (myoma): control group 1.1 (14 samples) and control group 2.1 (14 samples)
2. Premalignant samples (endometriosis): experimental group 1.2 (14 samples) and experimental group 2.2 (14 samples)

To ensure the statistical significance of the Mueller matrix polarization-interferometry method, we set the confidence interval value as $p \prec 0.05$.

To determine the representativeness of each sample (the number of samples in each of the groups 1.1, 1.2, 2.1, and 2.2), we calculated the standard deviation σ^2 of each of the statistical moments, Z_(i = 1; 2; 3; 4) (n), until its value satisfied the condition $\sigma^2 \le 0.025$. This condition was achieved when the number of samples in each group was $n = 14$.

From a morphological point of view, benign and premalignant tumors are characterized by different polycrystalline structures. Benign tumors (myoma) have a collagen and myosin fibrous network. Premalignant tumors (endometriosis) have a "developed" fibrous network of the connective tissue component, which is oriented in specific directions and scales [40]. Similar polarization manifestations of the polycrystalline newly formed fibrillar growth networks of other types of biological tissues have been studied using laser polarimetry in a number of other publications [20, 21, 34–36].

The combined selection, for studying two types of uterine tissue samples, allows for the comparative investigation of their effectiveness under different scattering conditions by two methods: Stokes polarimetry and phased selection of polarization components $(\{\Lambda(\alpha_j;\rho_j)+\Psi(\beta_j;\delta_j)\}+\Lambda^n(\sum_{j=1}^{n}q(\rho_j))+\Psi^n(\sum_{j=1}^{n}g(\delta_j))+\{\Lambda I(\alpha_j^n;\varphi_j)+\Psi I(\beta_j^n;\varphi_j)\})$ of the diffuse field and the extraction of the minimally scattered (most diagnostically important) component $\{\Lambda(\alpha_j;\rho_j)+\Psi(\beta_j;\delta_j)\}$.

Obtaining optically thin histological sections with controlled parameters of single scattering using a microtome is a complex and not always achievable task. It is further justified that polarization-interference scanning of the biological layer object fields (Equation 18) can use optically thick samples.

The results, obtained from the methods of Stokes-polarimetric mapping and polarization-interference layered-phase scanning of object field research sample tissues from the female reproductive system, were analyzed. The informational analysis involves the use of operational characteristics from evidence-based medicine [41].

6 Experimental results and discussion

This section of the article provides a systematic representation of the experimental results along with their discussion, focusing on the structure of azimuths $\alpha(m,n)$ and ellipticity $\beta(m,n)$ maps within the integral, layered, and polarization-inhomogeneous object fields of diffusive samples from the female reproductive system (see Table 1).

6.1 Integral- and layered-polarization azimuth maps

Figure 2 shows the following: integral-polarization azimuth $\alpha(m,n)$ map fragments (1) and (2); layered phase-polarization azimuth $\alpha(\theta_k,m,n)$ maps for $\theta_k = \pi/4$ fragments (5) and (6) and for $\theta_k = \pi/8$ fragments (9) and (10); histogram $G(\alpha)$ fragments (3) and (4); histogram $G(\theta_k = \pi/4,\alpha)$ fragments (7) and (8); and $G(\theta_k = \pi/8,\alpha)$ fragments (11) and (12).

The analysis of the obtained data revealed the following:

1. Coordinate inhomogeneity and individual statistical structure of the integral (Figure 2; fragments (1) and (2)) and layered phase (Figure 2; fragments (5) and (6) and (9) and (10)) azimuth polarization maps of the myoma and endometrium histological sections
2. Asymmetric histograms of the integral ($G(\alpha)$; Figure 2; fragments (3) and (4)) and layered phase ($G(\theta_k = \pi/4,\alpha)$, $G(\theta_k = \pi/8,\alpha)$; Figure 2; fragments (7) and (8) and (11) and (12))

The statistical analysis results of the polarization azimuth maps $\alpha(m,n)$ and $\alpha(\theta_k,m,n)$ are presented in Table 2.

It shows the following:

- All the first- and fourth-order statistical moments that characterize the histograms (α) and $G(\theta_k = \pi/4,\alpha), G(\theta_k = \pi/8,\alpha)$ are different from zero, $Z_{i=1,2,3,4}((\alpha),(\theta_k = \pi/4,\alpha),(\theta_k = \pi/8,\alpha)) \neq 0$
- The higher-order statistical moments that characterize the asymmetry and excess of distributions $G(\alpha)$ i $G(\theta_k = \pi/4,\alpha), G(\theta_k = \pi/8,\alpha)$ are the most sensitive to changes in the polarization azimuth map
- Value change scenarios of the first- and fourth-order statistical moments, which characterize the polarization azimuth maps of myoma (M) and endometrium (E) histological sections, $\begin{pmatrix} Z_{i=1,2}(\mathrm{M},(\alpha),(\theta_k)) < Z_{i=1,2}(\mathrm{E},(\alpha),(\theta_k)) \\ Z_{i=3,4}(\mathrm{M},(\alpha),(\theta_k)) > Z_{i=3,4}(\mathrm{E},(\alpha),(\theta_k)) \end{pmatrix}$

From a physical point of view, the obtained results can be attributed to the pathological alterations in the connective tissue component. These alterations lead to an increase in the "neo-formed" structural anisotropy (the relationship between (2) and (5)) of collagen networks through the geometric and orientational growth of protein fibers. As a consequence, there is an enlargement in the distribution of the orientations of the optical axes $\Delta\rho(m,n) \to max$ of fibrillar crystals, along with their birefringence $\delta(m,n) = \frac{2\pi}{\lambda}\Delta nd(m,n)$.

The aforementioned precancerous pathological changes will lead to an increase in the mean Z_1 $(\alpha,\rho,\delta) \uparrow$ and variance Z_2 $(\alpha,\rho,\delta) \uparrow$ of the polarization azimuth fluctuations in the

10.3389/fphy.2023.1302254

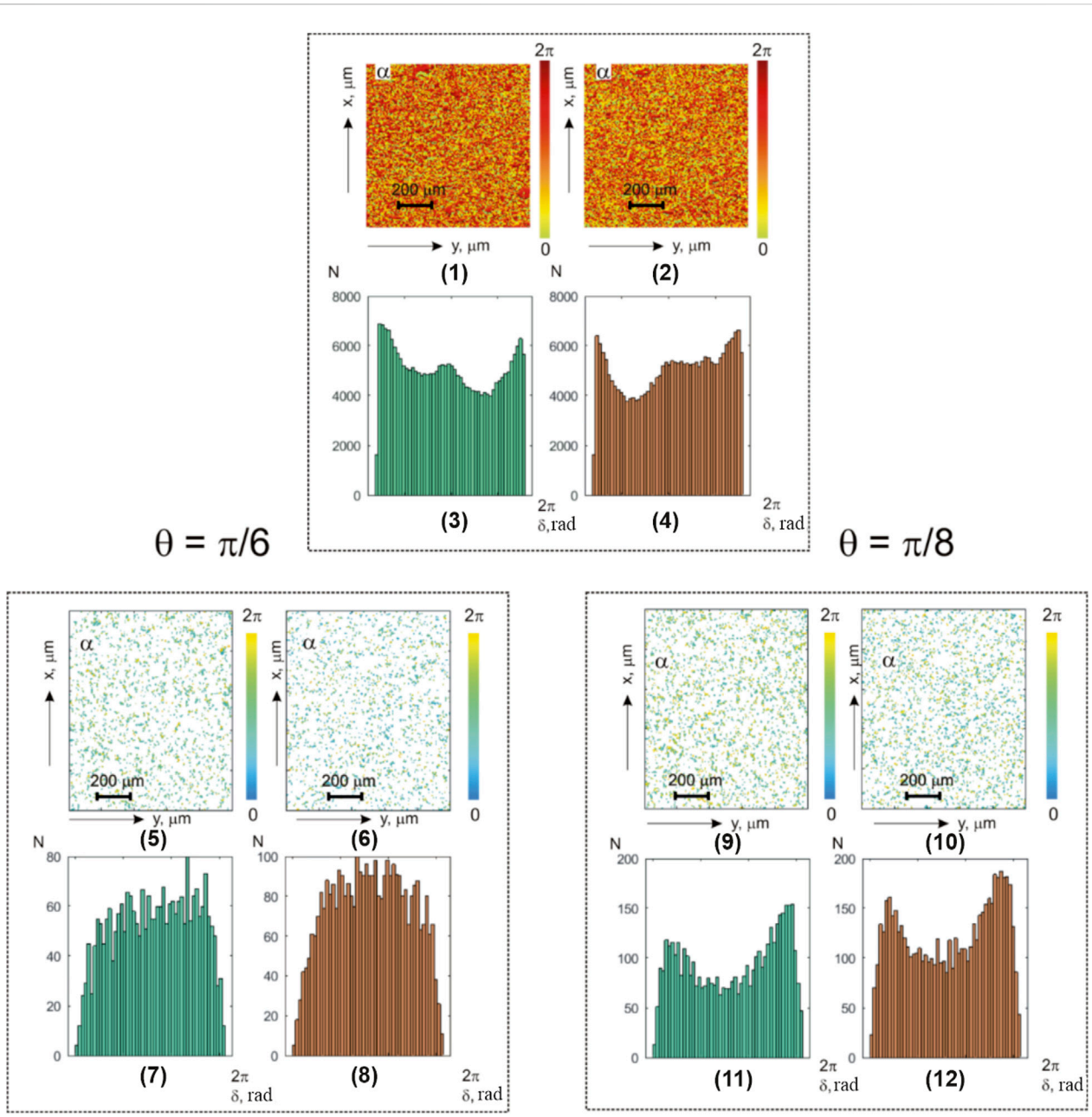

FIGURE 2
Coordinate and statistical structure of azimuth-polarization maps for optically thin ($\tau \leq 0.01$) myoma and precancerous endometrium histological sections, left and right columns, respectively (explanation in the text).

TABLE 2 Balanced accuracy threshold levels.

Diagnostic accuracy assessment	Accuracy *Ac*, %	Color
Unsatisfactory	≤ 80	
Satisfactory	81–85	
Good	86–90	
Very good	91–95	
Excellent	> 95	

corresponding carcinoma biopsy histological section microscopic image. At the same time, the magnitude of the third- and fourth-order statistical moments that characterize the asymmetry and excess of the distributions $\alpha(m,n)$ will decrease (relation (22)), i.e., $Z_{3,4}\ (\alpha,\rho,\delta) \downarrow$ (Table 3).

The results of the information analysis (in relation to (23)–(25)) revealed a set of diagnostic markers and the following accuracy levels in the benign and precancerous condition differential diagnoses:

- Integrated-polarization azimuth maps: satisfactory level $Ac\,(Z_4\,(\alpha)) = 82.1\%$

TABLE 3 Statistical moments of the first and fourth orders characterizing the layer-by-layer-polarization azimuth maps.

Parameter	Group 1	Group 2	*Ac*, %
Z_1	0.105 ± 0.006	0.12 ± 0.007	75
Z_2	0.81 ± 0.04	0.72 ± 0.04	75
Z_3	0.91 ± 0.05	0.84 ± 0.05	78.6
Z_4	1.21 ± 0.07	0.97 ± 0.051	82.1
Phase shift $\theta = \pi/4$			
Z_1	0.93 ± 0.049	1,04 ± 0.05	78.6
Z_2	0.69 ± 0.038	0.75 ± 0.04	78.6
Z_3	0.76 ± 0.041	0.61 ± 0.03	85.7
Z_4	0.88 ± 0.047	0.71 ± 0.04	85.7
Phase shift $\theta = \pi/8$			
Z_1	0.74 ± 0.04	0.86 ± 0.05	82.1
Z_2	0.76 ± 0.04	0.91 ± 0.05	82.1
Z_3	1.12 ± 0.06	0.88 ± 0.05	89.2
Z_4	1.33 ± 0.07	1.04 ± 0.05	89.2

- Layered-polarization azimuth maps: good level $Ac\left(Z_{3,4}\left(\alpha, \theta_k = \pi/4, \pi/8\right)\right) = 85.7\% - 89.2\%$

6.2 Integral- and layered-polarization ellipticity maps

Figure 3 presents the investigation results of the benign myoma and precancerous endometriosis object fields (notations are similar to those in Figure 2).

The analysis of the obtained data revealed a united heterogeneous topographic and coordinate structure of the experimentally obtained integral- (Figure 3; fragments (1) and (2)) and layer-by-layer-polarization ellipticity maps (Figure 3; fragments (5) and (6) and (9) and (10)).

Table 4 illustrates the statistical analysis results of the $\beta(m,n)$ and $\beta(\theta_k, m, n)$ maps.

Here, we found the following:

- Distinct from the normal and individual statistical distributions of the polarization parameters, $Z_{i=1,2,3,4}\left((\beta), (\theta_k = \pi/4, \beta), (\theta_k = \pi/8, \beta)\right) \neq 0$.
- Diagnostic markers of the benign and precancerous changes: higher-order statistical points that characterize the asymmetry and excess of the distributions $G(\beta)$ and $G(\theta_k = \pi/4, \beta), G(\theta_k = \pi/8, \beta)$.
- Precancerous changes in the polycrystalline component of the endometrial samples (group 2) are accompanied by an increase in the mean $Z_1\ (\beta, \rho, \delta) \uparrow$ and variance $Z_2\ (\beta, \rho, \delta) \uparrow$. At the same time, the magnitude of the third- and fourth-order statistical moments decreases, $Z_{3,4}\ (\beta, \rho, \delta) \downarrow$ and $\left(\begin{array}{c} Z_{i=1,2}(\mathrm{M}, (\beta), (\theta_k)) < Z_{i=1,2}(\mathrm{E}, (\beta), (\theta_k)); \\ Z_{i=3,4}(\mathrm{M}, (\beta), (\theta_k)) > Z_{i=3,4}(\mathrm{E}, (\beta), (\theta_k)) \end{array}\right)$.

Information analysis results revealed a significant increase in the accuracy of the differential diagnosis of the benign and precancerous conditions in the female reproductive sphere:

- The integral-polarization ellipticity maps show a good level of accuracy: $Ac\left(Z_{3,4}(\beta)\right) = 85.7\%$
- The layer-wise phase-polarization ellipticity maps demonstrate the following accuracy levels: good level $Ac\left(Z_3(\beta, \theta_k = \pi/4)\right) = 89.2\%$, very good level $Ac\left(Z_4(\beta, \theta_k = \pi/8)\right) = 91.7\%$, and very good level $Ac\ \left(Z_{3,4}(\beta, \theta_k = \pi/8)\right) = 92.8\%$
- Starting from $\theta_k \leq \pi/8$, the balanced accuracy remains practically unchanged, $Ac\left(Z_{3,4}(\beta, \theta_k = \pi/8)\right) \approx const$

From a physical point of view, the discovered regularities can be attributed to the fact that for $\theta_k \leq \pi/8$, the "single-scattering" regime occurs within the volume of optically thin biological layers. As a result, the maximum possible polarimetric differential diagnosis accuracy of the female reproductive system benign and precancerous states is achieved.

6.3 Optically thick-layer polarization azimuth maps

Figure 4 displays the maps and histograms illustrating the distribution of polarization azimuth values $\alpha(m,n)$ in the microscopic images of the histological sections from diffuse benign uterine fibroids and precancerous endometriosis tissues. The notations are consistent with those employed in Figures 2, 3.

The analysis of the obtained results revealed, similar to the studies on optically thin layers, topographic and coordinate inhomogeneity in the integral (Figure 4; fragments (1) and (2))-

10.3389/fphy.2023.1302254

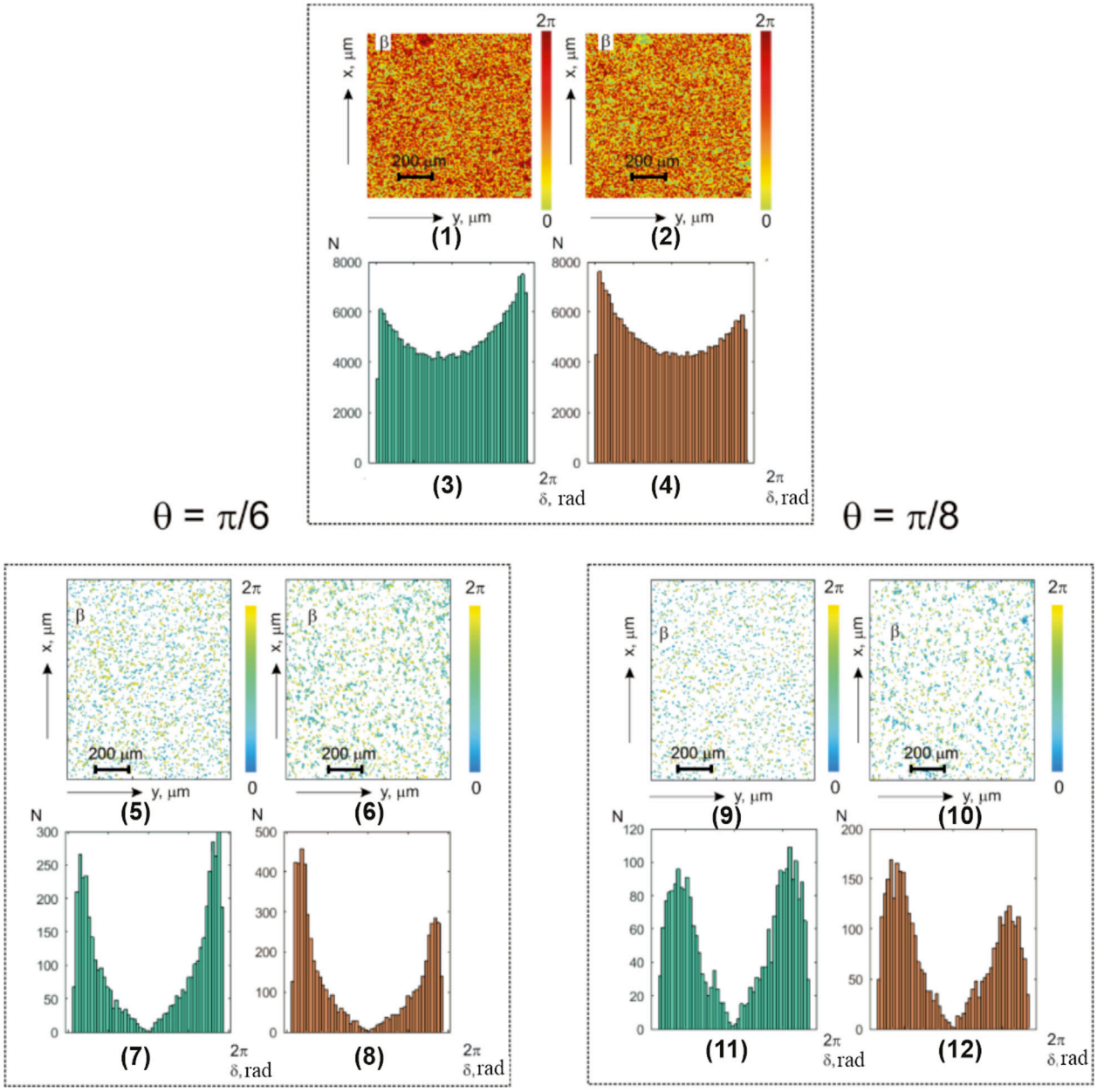

FIGURE 3
Coordinate and statistical structure of layered ellipticity-polarization maps for optically thin ($\tau \leq 0.01$) myoma and precancerous endometrium histological sections, left and right columns, respectively (explanation is given in the text).

and layer-wise phase (Figure 4; fragments (5) and (6) and (9) and (10))-polarization azimuth maps in benign and precancerous uterine tissues of optically thick-histological section microscopic images.

The research results on the diagnostic sensitivity of integral- and phase-polarization azimuth mapping in optically thick-histological section microscopic images of both groups showed predominant secondary interference mechanisms' influence. These mechanisms form the elliptically polarized diffuse component of the object field in almost all phase planes (except for $\theta_k \leq \pi/8$).

As a result, unsatisfactory levels of diagnostic sensitivity for integral-polarization azimuth maps were obtained (Table 2), $Ac\left(Z_{3,4}\left(\alpha\right)\right) < 80\%$.

Layer-by-layer phase-polarization azimuth maps illustrate the improvement in accuracy to a satisfactory level, $Ac\left(Z_{3,4}\left(\alpha, \theta_k = \pi/8\right)\right) = 85.7\%$.

6.4 Optically thick-layer polarization ellipticity maps

Figure 5 presents the polarization maps $\beta\left(m,n\right)$ of uterine tissue histological sections.

The analysis of the obtained results revealed a sufficiently similar, albeit complex, topographic and coordinate structure of polarization

TABLE 4 First- and fourth-order statistical moment characterization of the layer-by-layer-polarization azimuth maps for optically thick histological sections.

Parameter	Group 1	Group 2	*Ac*, %
Z_1	0.51 ± 0.03	0.59 ± 0.03	71.4
Z_2	0.72 ± 0.04	0.79 ± 0.04	75
Z_3	0.63 ± 0.03	0.56 ± 0.04	78.6
Z_4	0.82 ± 0.04	0.76 ± 0.05	78.6
Phase shift $\theta = \pi/4$			
Z_1	0.71 ± 0.04	0.78 ± 0.04	75
Z_2	0.77 ± 0.04	0.86 ± 0.05	78.6
Z_3	0.58 ± 0.03	0.47 ± 0.03	78.6
Z_4	0.42 ± 0.02	0.34 ± 0.02	82.1
Phase shift $\theta = \pi/8$			
Z_1	0.44 ± 0.02	0.49 ± 0.03	82.1
Z_2	0.59 ± 0.03	0.67 ± 0.04	82.1
Z_3	0.71 ± 0.04	0.82 ± 0.04	85.7
Z_4	0.88 ± 0.05	0.97 ± 0.05	85.7

TABLE 5 Statistical moments of the first- and fourth-order characterization of the layer-by-layer ellipticity-polarization maps for optically thick histological sections.

Parameter	Group 1	Group 2	*Ac*, %
Z_1	0.27 ± 0.01	0.31 ± 0.02	67.9
Z_2	0.33 ± 0.02	0.37 ± 0.02	71.4
Z_3	0.42 ± 0.02	0.34 ± 0.03	75
Z_4	0.55 ± 0.05	0.48 ± 0.04	78.6
Phase shift $\theta = \pi/4$			
Z_1	0.15 ± 0.008	0.18 ± 0.01	82.1
Z_2	0.17 ± 0.009	0.22 ± 0.01	82.1
Z_3	0.75 ± 0.04	0.66 ± 0.04	85.7
Z_4	0.92 ± 0.05	0.81 ± 0.04	85.7
Phase shift $\theta = \pi/8$			
Z_1	0.11 ± 0.006	0.14 ± 0.008	82.1
Z_2	0.15 ± 0.008	0.19 ± 0.01	85.7
Z_3	1.38 ± 0.07	1.01 ± 0.05	85.7
Z_4	2.21 ± 0.1	1.68 ± 0.09	92.8

ellipticity maps (Figure 5; fragments (1), (2), (5), and (6) and (9) and (10)).

Table 5 illustrates the statistical analysis results of the polarization ellipticity maps $\beta(m,n)$ and $\beta(\theta_i,m,n)$.

Within the framework of the statistical approach for the analysis of experimental data, we found the following:

- Different from the normal statistical distributions of polarization ellipticity maps, $Z_{i=1,2,3,4}((\beta),(\theta_k=\pi/4,\beta),(\theta_k=\pi/8,\beta))\neq 0$
- Diagnostic markers are higher-order statistical moments that characterize the asymmetry and excess of distributions $G(\beta)$ and $G(\theta_k=\pi/4,\beta), G(\theta_k=\pi/8,\beta)$

10.3389/fphy.2023.1302254

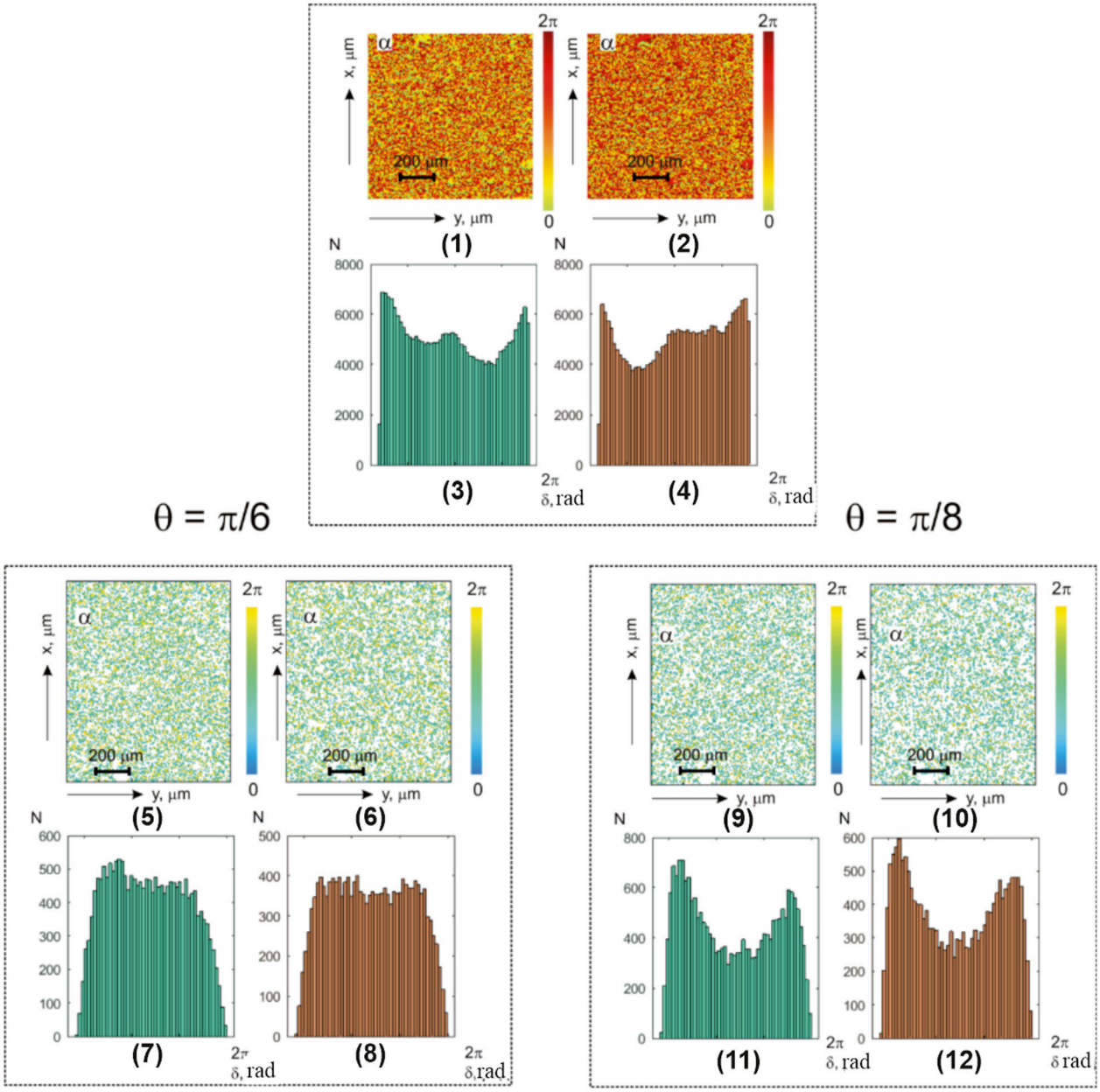

FIGURE 4
Coordinate and statistical structure of the layer-by-layer-polarization azimuth maps for optically thick ($\tau > 0.01$) myoma and precancerous endometrium histological sections, left and right columns, respectively (explanation is given in the text).

We already noted that the pathological changes in the polycrystalline component of diffuse endometrial samples from group 2 are accompanied by opposite scenarios of the transformation of the values of statistical markers, showing an increase in the average $Z_1\ (\beta, \rho, \delta) \uparrow$ and variance $Z_2\ (\beta, \rho, \delta) \uparrow$ and, conversely, a decrease of the third- and fourth-order statistical moments $Z_{3;4}\ (\beta, \rho, \delta) \downarrow$.

A comparative analysis of the layer-by-layer maps $\beta(\theta_i, m, n)$ revealed that as the value of θ_k decreases, there is a consistent dispersion $Z_2(\theta_k; \beta)$ decrease (up to three times) (Table 5). At the same time, the value of $Z_{3,4}\ (\beta, \rho, \delta)$ increases up to three to four times.

A further reduction of the parameter $\theta < \pi/8$ of the object field phase section practically does not lead to changes in the statistical structure of the polarization maps. This fact indicates that for such phase planes, the most "diagnostically favorable" mode of single scattering in the volume of uterine tissue diffuse layers is realized. Therefore, it is in the phase plane $\theta = \pi/8$ that we observe the greatest difference (40%–50%) between the statistical moments $Z_{3;4}(\theta_k; \beta)$, which characterize the distributions of $\Psi(\beta_j; \delta_j)$ in object fields of the samples of benign and precancerous uterine tissues.

As a result, for female reproductive sphere-diffuse tissue samples in precancerous conditions, the accuracy of the

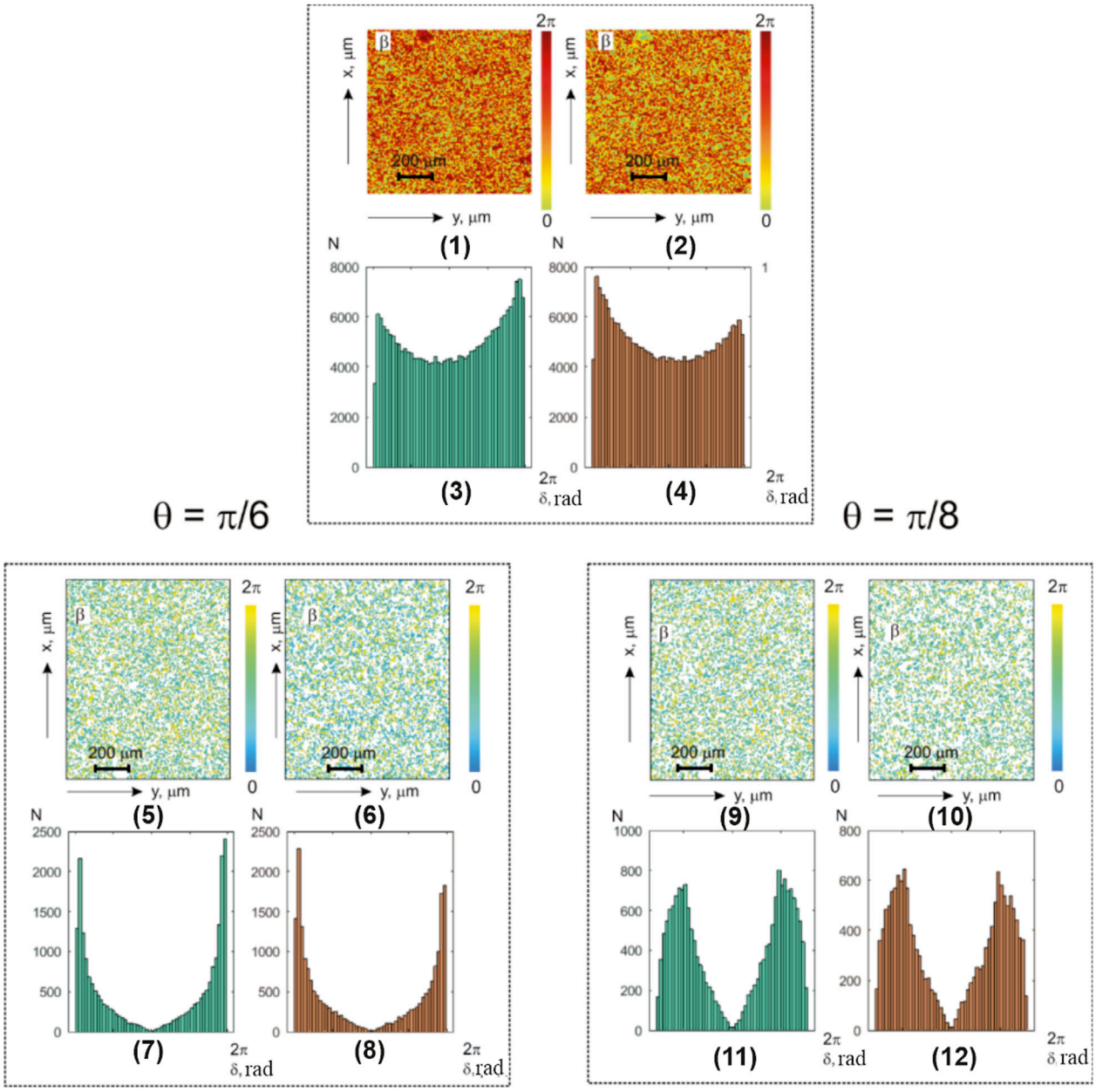

FIGURE 5
Coordinate and statistical structure of layer-by-layer-polarization ellipticity maps for optically thick ($\tau > 0.01$) myoma and precancerous endometrium histological sections, left and right columns, respectively (explanation is given in the text).

balanced differential diagnosis in the phase plane $\theta = \pi/8$ reaches the same level as that for optically thin samples (Table 4), $Ac\left(Z_{3,4}\left(\beta, \theta_k = \pi/8\right)\right) = 92.8\%$.

7 Conclusion

1. The experimental results of the diagnostic applications, employing vector-parametric polarization mapping and polarization-interference phase scanning methods on object fields of female reproductive sphere tissues, were presented and physically analyzed. This approach involves a layer-by-layer digital polarization map holographic reproduction, contributing to the differential diagnosis of benign (myoma) and precancerous (endometriosis) conditions.
2. For all types of pathology, it is an established complex, and for the individual statistics of integral- and layered-polarization maps, all statistical moments of the first and fourth orders, which characterize the histograms $G(\alpha, \beta)$ and $G(\theta_k = \pi/4, \alpha, \beta), G(\theta_k = \pi/8, \alpha, \beta)$, are different from zero, $Z_{i=1,2,3,4}\left(\left(\alpha, \beta\right), \left(\theta_k = \pi/4, \alpha, \beta\right), \left(\theta_k = \pi/8, \alpha, \beta\right)\right) \neq 0$.
3. The following maximum precancerous condition differential diagnosis accuracy levels using optically thin histological sections were revealed:

3.1. Integral-polarization azimuth maps: satisfactory $Ac(Z_4(\alpha)) = 82.1\%$

3.2. Layer-by-layer phase-polarization azimuth maps: good $Ac(Z_{3,4}(\alpha, \theta_k = \pi/4, \pi/8)) = 85.7\% - 89.2\%$

3.3. Integral-polarization ellipticity maps: good $Ac(Z_{3,4}(\beta)) = 85.7\%$

3.4. Layer-by-layer phase-polarization ellipticity maps: good $Ac(Z_3(\beta, \theta_k = \pi/4)) = 89.2\%$, very good $Ac(Z_4(\beta, \theta_k = \pi/8)) = 91.7\%$, and equivalent to very good $Ac(Z_{3,4}(\beta, \theta_k = \pi/8)) = 92.8\%$

4. For optically thick histological sections, the obtained results are given as follows:

4.1. The diagnostic sensitivity for integral-polarization azimuth maps was unsatisfactory, $Ac(Z_{3,4}(\alpha)) < 80\%$

4.2.Layer-wise phase-polarization azimuth maps demonstrated an improvement in the accuracy level to a satisfactory level, $Ac(Z_{3,4}(\alpha, \theta_k = \pi/8)) = 85.7\%$

5. The precancerous states of the female reproductive system diffuse tissue sample detection accuracy for polarization ellipticity maps in the phase plane $\theta = \pi 8$ reached a level similar to those of optically thin samples, $Ac(Z_4(\beta, \theta_k = \pi/8)) = 92.8\%$.

Data availability statement

The original contributions presented in the study are included in the article/Supplementary Material; further inquiries can be directed to the corresponding authors.

Ethics statement

The studies involving humans were approved by the Ethics Committee of the Bureau of Forensic Medicine of the Chernivtsi Region. The studies were conducted in accordance with the local legislation and institutional requirements. Written informed consent for participation was not required from the participants or the participants' legal guardians/next of kin because histologically verified preparations from the archive of the Bureau of Forensic Medicine of the Chernivtsi Region were used as the experimental samples.

Author contributions

AU: project administration, writing–original draft, and writing–review and editing. AD: investigation and writing–original draft. JZ: conceptualization, methodology, supervision, and writing–review and editing. OB: conceptualization, formal analysis, investigation, and writing–review and editing. MG: software, visualization, and writing–review and editing. YU: data curation, investigation, and writing–original draft. OL: formal analysis, investigation, and writing–review and editing. IG: investigation and writing–review and editing. CZ: data curation and writing–review and editing. VS: writing–review and editing, formal Analysis, visualization.

Funding

The authors declare that financial support was received for the research, authorship, and/or publication of this article. The authors acknowledge support from the National Research Foundation of Ukraine, Project 2022.01/0034, and the Scholarship of the Verkhovna Rada of Ukraine for Young Scientists and Doctors of Science.

Conflict of interest

The authors declare that the research was conducted in the absence of any commercial or financial relationships that could be construed as a potential conflict of interest.

Publisher's note

All claims expressed in this article are solely those of the authors and do not necessarily represent those of their affiliated organizations, or those of the publisher, the editors, and the reviewers. Any product that may be evaluated in this article, or claim that may be made by its manufacturer, is not guaranteed or endorsed by the publisher.

References

1. World Health Organisation. Classification of diseases (ICD) (2022). Available at: https://www.who.int/standards/classifications/classification-of-diseases.

2. Zondervan KT, Becker CM, Missmer SA. Endometriosis. *New Engl J Med* (2020) 382(13):1244–56. doi:10.1056/nejmra1810764

3. Agarwal SK, Chapron C, Giudice LC, Laufer MR, Leyland N, Missmer SA, et al. Clinical diagnosis of endometriosis: a call to action. *Am J Obstet Gynecol* (2019) 220(4): 354.e1–354.e12. doi:10.1016/j.ajog.2018.12.039

4. Johnson NP, Hummelshoj L, Abrao MS, Adamson GD, Allaire C, Amelung V, et al. Consensus on current management of endometriosis. *Hum Reprod* (2013) 28(6):1552–68. doi:10.1093/humrep/det050

5. de Boer JF, Milner TE. Review of polarization sensitive optical coherence tomography and Stokes vector determination. *J Biomed Opt* (2002) 7(3):359. doi:10.1117/1.1483879

6. Spandana KU, Krishna KM, Mazumder N. Polarization-resolved Stokes-Mueller imaging: a review of technology and applications. *Lasers Med Sci* (2019) 34(7):1283–93. doi:10.1007/s10103-019-02752-1

7. He Y, Li K, Li W, Qiu Y, Li D, Wang C, et al. Polarization coherency matrix tomography. *J Biophotonics* (2023) 16(9): e202300093. doi:10.1002/jbio.202300093

8. Yang D, Yuan Z, Hu M, Liang Y. Zebrafish brain and skull imaging based on polarization-sensitive optical coherence tomography. *J Biophotonics* (2022) 15(12): e202200112. doi:10.1002/jbio.202200112

9. Park JE, Zhou X, Kwon DY, Kim SW, Lee H, Jung MJ, et al. Application of polarization sensitive-optical coherence tomography to the assessment of phase retardation in subpleural cancer in rabbits. *Tissue Eng Regenerative Med* (2021) 18(1):61–9. doi:10.1007/s13770-020-00318-9

10. Willemse J, Maximilian GOG, Verbraak FD, de Boer JF. *In vivo* 3D determination of peripapillary scleral and retinal layer architecture using polarization-sensitive optical coherence tomography. *Translational Vis Sci Tech* (2020) 9(11):21–1. doi:10.1167/tvst.9.11.21

11. Baumann B, Augustin M, Lichtenegger A, Harper DJ, Muck M, Eugui P, et al. Polarization-sensitive optical coherence tomography imaging of the anterior mouse eye. *J Biomed Opt* (2018) 23(08):1. doi:10.1117/1.jbo.23.8.086005

12. Hariri LP, Adams DC, Applegate MB, Miller AJ, Roop BW, Villiger M, et al. Distinguishing tumor from associated fibrosis to increase diagnostic biopsy yield with polarization-sensitive optical coherence tomography. *Clin Cancer Res* (2019) 25(17): 5242–9. doi:10.1158/1078-0432.ccr-19-0566

13. Tao K, Sun K, Ding Z, Ma Y, Kuang H, Zhao H, et al. Catheter-based polarization sensitive optical coherence tomography using similar mueller matrix method. *IEEE Trans Biomed Eng* (2020) 67(1):60–8. doi:10.1109/tbme.2019.2908031

14. Burns JA, Kim KH, deBoer JF, Rox Anderson R, Zeitels SM. Polarization-sensitive optical coherence tomography imaging of benign and malignant laryngeal lesions. *Otolaryngol Head Neck Surg* (2011) 145(1):91–9. doi:10.1177/0194599811403078

15. Tuchin VV. *Tissue optics: light scattering methods and instruments for medical diagnosis*. Bellingham, Washington, USA: Spie Press (2015).

16. Ghosh N. Tissue polarimetry: concepts, challenges, applications, and outlook. *J Biomed Opt* (2011) 16(11):110801. doi:10.1117/1.3652896

17. Jacques SL. Polarized light imaging of biological tissues. In: *Handbook of biomedical Optics2*. Boca-Raton: CRC Press (2011). p. 649–69.

18. Layden D, Ghosh N, Vitkin IA. Quantitative polarimetry for tissue characterization and diagnosis. In: *Advanced biophotonics: tissue optical sectioning*. Boca-Raton: CRC Press (2013). p. 73–108.

19. Vitkin A, Ghosh N, de Martino A. Tissue polarimetry. In: Andrews DL, editor. *Photonics: scientific foundations, technology and applications. Goboken*. John Wiley and Sons, Ltd (2015). p. 239–321.

20. Angelsky OV, Ushenko YA, Ushenko A. Statistical, correlation, and topological approaches in diagnostics of the structure and physiological state of birefringent biological tissues. In: Tuchin VV, editor. *Handbook of photonics for biomedical science*. London: CRC Press, Taylor and Francis Publishing (2010). p. 283–322.

21. Ushenko YA, Boychuk TM, Bachynsky VT. Diagnostics of structure and physiological state of birefringent biological tissues: statistical, correlation and topological approaches. In: Tuchin VV, editor. *Handbook of coherent-domain optical methods: biomedical diagnostics, environmental monitoring, and materials science*. New York: Springer New York (2013). p. 107–48.

22. Gil JJ, Ossikovski R. *Polarized light and the mueller matrix approach*. Boca-Raton: CRC Press (2022).

23. Arteaga O, Kahr B. Mueller matrix polarimetry of bianisotropic materials [Invited]. *J Opt Soc America B-optical Phys* (2019) 36(8):F72–2. doi:10.1364/josab.36.000f72

24. Lee HR, Lotz C, Kai Groeber Becker F, Dembski S, Novikova T. Digital histology of tissue with Mueller microscopy and FastDBSCAN. *Appl Opt* (2022) 61(32):9616. doi:10.1364/ao.473095

25. Novikova T, Kim M, Lee HR, Ossikovski R, Malfait-Jobart A, Lamarque D. Optical diagnosis of gastric tissue biopsies with Mueller microscopy and statistical analysis. *J Eur Opt Soc Rapid Publications* (2022) 18(2):10. doi:10.1051/jeos/2022011

26. Lee HR, Li P, Sang T, Lotz C, Groeber-Becker F, Dembski S, et al. Digital histology with Mueller microscopy: how to mitigate an impact of tissue cut thickness fluctuations. *J Biomed Opt* (2019) 24(07):076004. doi:10.1117/1.JBO.24.7.076004

27. Li P, Lee HR, Chandel S, Lotz C, Groeber-Becker FK, Dembski S, et al. Analysis of tissue microstructure with Mueller microscopy: logarithmic decomposition and Monte Carlo modeling. *J Biomed Opt* (2020) 25(01):1. doi:10.1117/1.jbo.25.1.015002

28. Lee HR, Sang T, Li P, Lotz C, Groeber-Becker F, Dembski S, et al. *Mueller microscopy of anisotropic scattering media: theory and experiments*. France: Centre pour la Communication Scientifique Directe (2018).

29. Ma H, He H, Ramella-Roman JC. Mueller matrix microscopy. In: Ramella-Roman JC, Novikova T, editors. *Polarized light in biomedical imaging and sensing*. Cham: Springer (2023).

30. Peyvasteh M, Tryfonyuk L, Ushenko V, Syvokorovskaya A, Dubolazov AV, Vanchulyak O, et al. 3D Mueller-matrix-based azimuthal invariant tomography of polycrystalline structure within benign and malignant soft-tissue tumours. *Laser Phys Lett* (2020) 17(11):115606–6. doi:10.1088/1612-202x/abbee0

31. Ushenko V, Hogan B, Dubolazov A, Piavchenko G, Kuznetsov S, Ushenko A, et al. 3D Mueller matrix mapping of layered distributions of depolarisation degree for analysis of prostate adenoma and carcinoma diffuse tissues. *Scientific Rep* (2021)(1) 11. doi:10.1038/s41598-021-83986-4

32. Yu U, Sdobnov A, Dubolazov A, Grytsiuk M, Bykov A, Meglinski I, et al. Stokes-correlometry analysis of biological tissues with polycrystalline structure. *IEEE J Selected Top Quan Electro* (2019) 25(1):1–12. doi:10.1109/jstqe.2018.2865443

33. Ushenko VA, Hogan BT, Dubolazov A, Grechina AV, Boronikhina TV, Gorsky M, et al. Embossed topographic depolarisation maps of biological tissues with different morphological structures. *Scientific Rep* (2021)(1) 11. doi:10.1038/s41598-021-83017-2

34. Ushenko VA, Sdobnov A, Mishalov WD, Dubolazov AV, Олар OV, Bachinskyi VT, et al. Biomedical applications of Jones-matrix tomography to polycrystalline films of biological fluids. *J Innovative Opt Health Sci* (2019) 12(06):12. doi:10.1142/s1793545819500172

35. Ushenko AG, Dubolazov OV, Ushenko VA, Oyu N, Olar OV. Fourier polarimetry of human skin in the tasks of differentiation of benign and malignant formations. *Appl Opt* (2016) 55(12):B56. doi:10.1364/ao.55.000b56

36. Peyvasteh M, Dubolazov A, Popov A, Ushenko A, Meglinski I, Meglinski I. Two-point Stokes vector diagnostic approach for characterization of optically anisotropic biological tissues. *J Phys D* (2020) 53(39):395401–1. doi:10.1088/1361-6463/ab9571

37. Marchesini R, Bertoni A, Andreola S, Melloni E, Sichirollo AE. Extinction and absorption coefficients and scattering phase functions of human tissues *in vitro*. *Appl Opt* (1989) 28(12):2318–24. doi:10.1364/ao.28.002318

38. Edwards DK, Gier JT, Nelson KE, Roddick RD. Integrating sphere for imperfectly diffuse samples. *J Opt Soc America* (1961) 51(11):1279–9. doi:10.1364/josa.51.001279

39. Goodman JW. Laser speckle and related phenomena. In: Dainty JC, editor. *Topics in applied Physics*. Heidelberg: Springer-Verlag Berlin (1975). p. 9–75.

40. Rogers PAW, D'Hooghe TM, Fazleabas A, Gargett CE, Giudice LC, Montgomery GW, et al. Priorities for endometriosis research: recommendations from an international consensus workshop. *Reprod Sci* (2009) 16(4):335–46. doi:10.1177/1933719108330568

41. Robinson SP. *Principles of forensic medicine*. Cambridge: Cambridge University Press (1996).